Electrochimica Acta 432 (2022) 141162

Contents lists available at ScienceDirect

Electrochimica Acta

journal homepage: www.journals.elsevier.com/electrochimica-acta

Anodic Sb_2S_3 electrodeposition from a single source precursor for resistive random-access memory devices

A.G. Wallace [a,*], R.P. King [a], N. Zhelev [a], A.H. Jaafar [b,c], W. Levason [a], R. Huang [b], G. Reid [a], P. N. Bartlett [a,*]

[a] School of Chemistry, University of Southampton, Southampton SO17 1BJ, United Kingdom
[b] Electronics and Computer Science, University of Southampton, Southampton SO17 1BJ, United Kingdom
[c] Now at School of Physics and Astronomy, University of Nottingham, Nottingham NG7 2RD, United Kingdom

ARTICLE INFO

Keywords:
Antimony sulfide
Electrodeposition
Single source electrodeposition precursor
Resistive random-access memory

ABSTRACT

In this paper we report the use of $Na_3[SbS_4].9H_2O$ as a single source precursor for the electrodeposition of Sb_2S_3 from aqueous electrolyte at pH 9.1. We present the electrochemistry of the $[SbS_4]^{3-}$ anion and the redox processes observed for the deposited Sb_2S_3 film. We show that an amorphous Sb_2S_3 film can be deposited by anodic electrodeposition onto glassy carbon and that the by-product that accompanies this deposition can be avoided by using a suitable pulse plating approach. Raman spectroscopy and grazing incidence X-ray diffraction were used to characterise the deposits and to show that good quality crystalline films of Sb_2S_3 are produced on annealing.

The crystalline Sb_2S_3 films were screened for application in Resistive Random-Access Memory, and it was demonstrated that crystalline Sb_2S_3 films display typical bipolar resistive switching behaviour, and that the resistance ratio between the high resistance state and the low resistance state is approximately one order of magnitude at 1.5 V, which is sufficient for memory applications. A mechanism for the resistive switching is also proposed.

1. Introduction

The antimony chalcogenide family (Sb–S, Sb–Se, and Sb–S–Se) has garnered a significant level of attention in recent years, with Sb_2S_3 in particular being regarded as a very promising material. Sb_2S_3 has a band gap of approximately 1.7 eV and a high absorption coefficient, which makes it an attractive candidate for use in light sensitizers in both solar cells and photoelectrochemical devices [1–6]. Furthermore, with a theoretical capacity of 946 mA h g^{-1}, Sb_2S_3 has also attracted interest as a possible anode material for Li-ion and Na-ion batteries, and with a maximum specific capacitance of 248 F g^{-1}, it could be used for supercapacitor applications [7–11]. In addition, antimony and sulfur are quite abundant elements, and Sb_2S_3 possesses a relatively low toxicity and a good stability against air and moisture [2,12,13]. As such, the development of effective Sb_2S_3 film preparation protocols is of great interest.

A range of different methods for Sb_2S_3 film preparation have been reported in the literature. Examples include atomic layer deposition [14], sputtering [15], spin coating [16], chemical bath deposition [17], and electrodeposition [18–21]. Electrodeposition in particular is an appealing approach for materials deposition, owing to its simplicity, high tunability, and its potential to be much more economical than other deposition techniques [22,23]. While electrodeposition has already been reported in the literature to be an effective way to prepare Sb_2S_3 films, all existing reports of Sb_2S_3 electrodeposition make use of two or more precursor salts, which can add both complexity and cost to the process [18–21]. Furthermore, all previously reported Sb_2S_3 electrodeposition methods required cathodic potentials and acidic electrolytes, which can limit substrate options and scale-up [18–21]

Resistive random-access memory (RRAM) devices are considered as one of the most promising candidates for next generation non-volatile memory applications due to their unique characteristics, such as high switching speeds, low power consumption, and long data retention and endurance capabilities [24–29]. Resistive switching has been observed in oxides, chalcogenides, organic, and organic-inorganic hybrid materials [30]. We have also previously reported the resistive switching behaviour from an electrodeposited Te-rich GeSbTe based memory device [24]. To the best of our knowledge there are no studies on the

* Corresponding authors.
E-mail addresses: A.G.Wallace@soton.ac.uk (A.G. Wallace), P.N.Bartlett@soton.ac.uk (P.N. Bartlett).

https://doi.org/10.1016/j.electacta.2022.141162
Received 7 June 2022; Received in revised form 4 August 2022; Accepted 7 September 2022
Available online 10 September 2022

fabrication of resistive switching memory devices based on electrodeposited Sb_2S_3.

In this work, we investigate the electrochemistry of the $[SbS_4]^{3-}$ anion in aqueous solution and use the findings to develop a protocol that allows for the deposition of an amorphous Sb_2S_3 film, which can then be crystallised by annealing. This procedure for Sb_2S_3 electrodeposition uses a single source precursor, anodic potentials, and non-acidic conditions. The resulting crystalline Sb_2S_3 films were then screened for RRAM applications, and it was found that they demonstrate typical bipolar resistive switching behaviour and that the resistance ratio between the high resistance state (HRS) and the low resistance state (LRS) is approximately one order of magnitude at 1.5 V, which is adequate for use in a memory device. The resistive switching mechanism is then shown to occur via the solid-state electrolyte effect.

2. Experimental

2.1. Preparation of $Na_3[SbS_4].9H_2O$ precursor

$Na_3[SbS_4].9H_2O$ was prepared using the literature method [31]. Sb_2S_3 (7.50 g, 2.20 mmol, from Sigma Aldrich) was added to a beaker and mixed with 60 mL of 20% (w/w) NaOH in water. Sulfur (4.24 g, 13.0 mmol) was added to this solution, the mixture was boiled while stirring until the solution changed from an orange-red colour to yellow. The volume of the resulting solution was reduced by half and allowed to cool to room temperature. After approximately 16 h, yellow crystals formed. The resultant crystals were collected and washed with isopropyl alcohol (3 × 20 mL) and diethyl ether (3 × 20 mL) and then dried in vacuo. Yield 7.30 g (76%). IR (Nujol/cm^{-1}): ν = 390 s (Sb-S). Raman (cm^{-1}): ν = 378, 363 (Sb-S). ^{121}Sb NMR (D_2O, 298 K): δ = 1033 ($[Sb\text{-}S_4]^{3-}$). The zero reference for the ^{121}Sb NMR spectroscopy was $[^nBu_4N][SbCl_6]$.

2.2. Characterisation of the precursor's electrochemistry and electrodeposition

All electrochemical characterisation experiments were carried out in a three-electrode cell. For voltammetry, the working electrode (WE) was a 3 mm diameter glassy carbon disc electrode that had been polished in a 1 μm alumina slurry before use. For electrodeposition, in order to obtain deposits that can be annealed, the WE was a glassy carbon plate (HTW Hochtemperatur-Werkstoffe GmbH) with its geometric surface area constrained to 0.50 cm^2. The counter electrode was a platinum rod with a surface area far exceeding that of the WE, and the reference electrode was a saturated calomel electrode (SCE). All potentials in this report are referenced against SCE. The background electrolyte was always 100 mM sodium citrate tribasic dihydrate (Sigma Aldrich) in ultrapure water (18.2 MΩ cm, Pur1te). The background electrolyte had a pH of 8.3, which became 9.1 upon the addition of 2 mM equivalent of $Na_3[SbS_4]$. All electrolytes were deoxygenated by bubbling with Ar before any electrochemical measurements. $SbCl_3$ (≥99.0%) was obtained from Sigma-Aldrich.

For comparison, Sb_2S_3 was also electrodeposited by holding a glassy carbon electrode at −0.6 V vs SCE in a solution of 2 mM $SbCl_3$ (≥99.0%, Merck), 10 mM sodium thiosulfate pentahydrate (>99%, Fisher Chemical), and 100 mM citric acid (≥99.7%, AnalaR) for 10 min. This approach is based on the established methods of electrodepositing Sb_2S_3 (separate precursors for S and Sb, acidic conditions, cathodic potentials) [19–21].

Electrochemical experiments were recorded using an Autolab PGStat30 potentiostat running NOVA 1.11.2 software.

For drop casting, a high-power ultrasonic probe was used to disperse 2 mg of Sb_2S_3 powder in 1 mL of 25% isopropyl alcohol/75% ultrapure water (by volume). 5 μL of this dispersion was then pipetted onto the surface of a GC disc electrode and the electrodes were left until the water/alcohol mixture had evaporated. It was found that neither carbon powder nor a binding agent was required to achieve an Sb_2S_3 loading on GC that yielded a useful and reproducible voltammogram.

For electrodeposition onto glassy carbon plates, the potential on the plate was held at 1 V vs SCE for 600 s in 2 mM $Na_3[SbS_4]$ in 100 mM of background electrolyte.

For pulse plating, the potential was stepped to 0.4 V vs SCE for 1 s, to −0.95 V vs SCE for 1 s and then to −0.3 V vs SCE for 1 s. 60 sets of steps in total were used for the electrodeposition onto the GC plates. This is referred to as the OxRed pulse protocol. The plating solution was 2 mM $Na_3[SbS_4]$ in 100 mM of background electrolyte.

Alternatively, pulse plating was carried out by stepping the potential to 0.4 V vs SCE for 1 s, and then to −0.15 V vs SCE for 2 s and repeating this loop 60 times. This is referred to as the control pulse protocol. The plating solution was 2 mM $Na_3[SbS_4]$ in 100 mM of background electrolyte.

2.3. Annealing of deposits

The samples were annealed in a quartz tube placed inside a tube furnace. Firstly, the sample was heated to 100 °C under a dynamic vacuum for 10 min to remove moisture from the system, the samples were then heated to 350 °C at approximately 0.1 mbar under a sulfur rich environment made by placing approximately 0.1 g of sulfur inside the quartz tube away from the electrodeposited sample.

2.4. Physical characterisation of deposits

Scanning electron microscopy (SEM) was performed using a Philips/FEI XL30 ESEM, with an acceleration voltage of 10 keV, and a working distance of 10 mm between a sample and the pole piece. Energy dispersive X-ray spectroscopy (EDX) was performed using a Thermo Scientific NORAN System Xray Microanalysis System, using a Thermo Scientific UltraDry 10 mm^2 detector.

X-ray diffraction (XRD) was performed using a Rigaku SmartLab diffractometer (Cu-K_α) with a grazing incidence angle of 1°, and Hypix 3000 detector in 1D mode. The resulting pattern were phase matched using the PDXL2 software package and matched to card 015,236 (stibnite) from the Inorganic Crystal Structure Database [32].

Raman spectroscopy was performed using a Renishaw InVia confocal Raman microscope coupled with a 785 nm laser diode, with a rated power of 500 mW. Spectra were obtained using 1% laser power, 10 accumulations per spectrum, and 5 s exposure for each scan.

2.5. Electrical device characterisation

The electrical characteristics were measured at room temperature and ambient pressure using a probe connected to a Keysight (B1500) system. For all measurements, the voltage was applied to the top contact (tungsten probe) whilst the bottom contact (glassy carbon) was grounded.

3. Results

3.1. Understanding the voltammetry of the $Na_3[SbS_4]$ precursor

The voltammetry of the $[SbS_4]^{3-}$ anion at a glassy carbon electrode is shown in Fig. 1.

Fig. 1 shows that when the potential on a glassy carbon electrode is made more positive than 0 V vs SCE, two electrooxidation processes are observed, with peaks at 0.38 V and 0.73 V, labelled A1 and A2 respectively. On the return scan, two sharp reduction peaks are observed at –0.92 V and −1.05 V, labelled C1 and C2 respectively. On the return positive scan oxidation processes are observed in the −0.8 to −0.4 V region (A3), followed by an oxidation peak at −0.32 V (A4), and then a slight oxidation current in the −0.1 to 0.05 V region (A5). Process A1 is then observed to occur at a less positive potential than on the first scan.

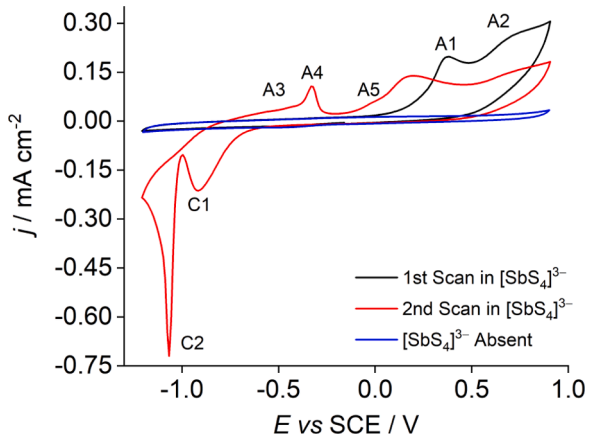

Fig. 1. Voltammetry of 2 mM $Na_3[SbS_4].9H_2O$ in 100 mM HOC(COONa)$(CH_2COONa)_2{\cdot}2H_2O$, pH 9.1. The first scan (black trace) and the second scan (red trace) are shown. The potential on the electrode was swept from −0.15 V to −1.2 V vs SCE, and then to 0.9 V vs SCE at 10 mV s^{-1}. A background voltammogram where no $Na_3[SbS_4].9H_2O$ was added to the electrolyte is included (blue trace) (For interpretation of the references to color in this figure legend, the reader is referred to the web version of this article.).

Based on the evidence that we present below, we assign processes A1 and A2 to the deposition of Sb_2S_3 and a by-product (most likely an antimony oxide/hydroxide) respectively. On the cathodic scan, processes C1 and C2 are, respectively, the electroreduction of the anodically deposited by-product and the electroreduction of deposited Sb_2S_3 to Sb (0) and aqueous phase sulfur species, process A3 is the oxidation of aqueous phase sulfur species released by process C2, process A4 is the oxidative stripping of Sb(0), and process A5 is the oxidation of any Sb(0) not stripped in A4 into some sort of antimony oxide/hydroxide.

3.2. Anodic electrodeposition

As shown in Fig. 1, if the potential is initially swept negative from −0.15 V (approximately the open circuit potential) to −1.2 V vs SCE, the current profile is indistinguishable from a voltammogram run in the absence of the $[SbS_4]^{3-}$ anion indicating that no reduction of $[SbS_4]^{3-}$ occurs. However, at potentials more positive than 0.05 V vs SCE, electrooxidation is observed in the voltammetry, and a peak (A1) appears at 0.38 V vs SCE. There is then a second oxidation peak (A2) at 0.74 V vs SCE. If the potential is held positive of 0.1 V vs SCE, a blue deposit begins to form on the electrode (SI, Fig. S1).

To study this deposit in greater detail, glassy carbon plates were held at 1.0 V vs SCE and the resulting deposits were annealed. The deposition potential was chosen based on the voltammetry on the glassy carbon plate electrodes (see SI, Fig. S2). Fig. 2a shows an SEM image of the deposit before annealing, a continuous film can be seen across the entire exposed surface of the plate. EDX spectra (Fig. 3) of several deposits

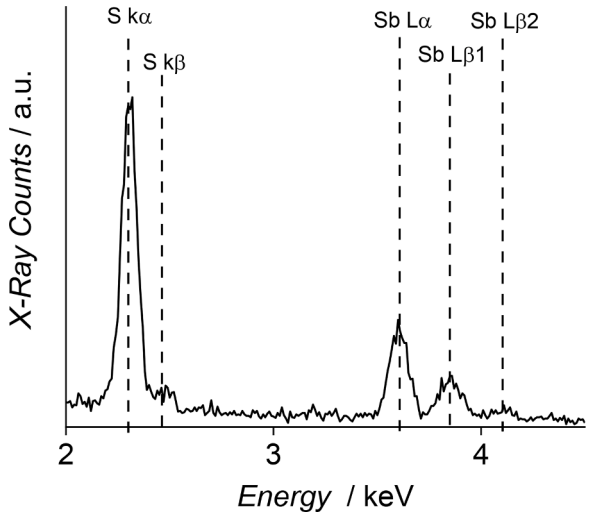

Fig. 3. EDX spectrum of the Sb_2S_3 deposit on glassy carbon, conditions as in Fig. 2. The full spectrum is given in the supplementary information, Fig. S4.

reveals that they consist of Sb and S in a 2:3 ratio (each recorded Sb:S ratio was within experimental error of an Sb:S ratio recorded on an Sb_2S_3 calibration pellet). Fig. 2b shows an SEM image of the film after annealing, the annealing process appears to have caused the formation of islands of Sb_2S_3 across the plate. These islands are thought to form due to the by-product of anodic Sb_2S_3 deposition being unstable under the annealing conditions.

Raman spectra of the deposits before and after annealing were recorded using a 785 nm laser excitation source. Fig. 4 shows the Raman spectra obtained for annealed deposits. The peaks are well defined, indicating that annealing causes the sample to crystalize. Well-resolved Raman bands are observed at 129, 156, 195, 239, 282, and 311 cm^{-1}, corresponding to the Sb_2S_3 stibnite phase, with the bands at 282 and 311 cm^{-1} arising due to the symmetric vibration of the Sb_2S_3 pyramidal units having C_{3v} symmetry [1–4,13,33]. The Raman spectra obtained for deposits that had not been annealed (see SI, Fig. S3) showed a broad feature at approximately 300 cm^{-1}, which is indicative of amorphous Sb_2S_3 [33].

The XRD patterns of the annealed deposits, Fig. 5, are largely dominated by the peaks from the glassy carbon substrate, but when the diffraction from the glassy carbon is subtracted from the signal obtained from annealed Sb_2S_3 on glassy carbon, peaks at $2\theta = 15.6$, 17.6, 25.2, 28.8, and 35.7° are observed, corresponding to the (200), (120), (130), (211), and (240) planes of Sb_2S_3 respectively [2,13]. The XRD pattern of an annealed Sb_2S_3 deposit on glassy carbon before the glassy carbon signal was subtracted, along with the XRD pattern of a clean glassy carbon plate, are shown in Fig. S5 supplementary information. No peaks are observed for XRD measurements on samples that have not be

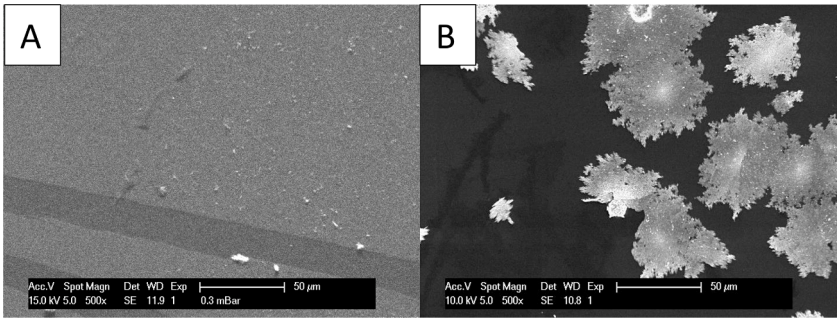

Fig. 2. SEM images of Sb_2S_3 deposited onto a glassy carbon plate by holding the plate at 1 V vs SCE for 10 min in 2 mM $Na_3[SbS_4].9H_2O$ in 100 mM HOC(COONa)$(CH_2COONa)_2{\cdot}2H_2O$, pH 9.1; (a) before annealing and (b) after annealing at 350 °C and 0.1 mbar in a sulfur rich environment.

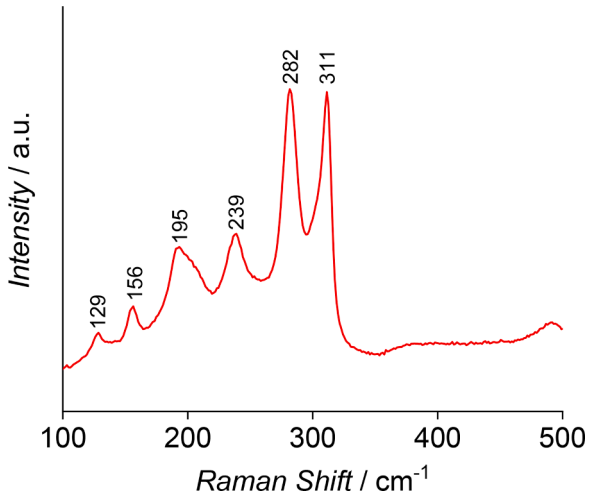

Fig. 4. Raman spectrum of an annealed Sb_2S_3 film on glassy carbon (deposition conditions as in Fig. 2). Annealing was performed by heating the sample at 350 °C at 0.1 mbar in a sulfur rich environment.

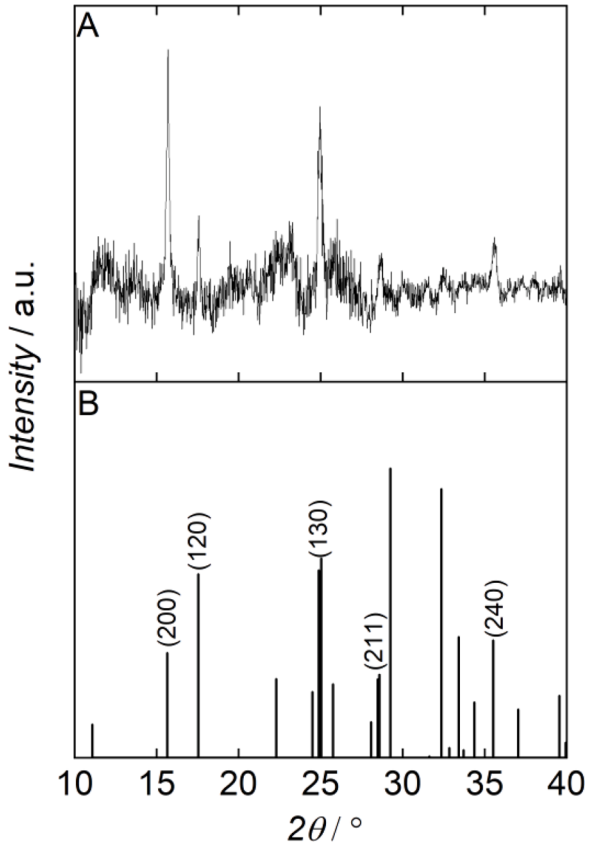

Fig. 5. (a) XRD pattern (where the signal from the glassy carbon has been subtracted) of an annealed Sb_2S_3 film electrodeposited onto a glassy carbon plate (conditions as in Fig. 4). (b) XRD pattern of Sb_2S_3 obtained from the Inorganic Crystal Structure Database [32].

annealed, further showing that the as-deposited films are amorphous.

Taken together this evidence shows that process A1 is the anodic deposition of Sb_2S_3 from the $[SbS_4]^{3-}$ anion. Given that, according to the Pourbaix diagram, the stable form for sulfur under these conditions is sulfate [34,35] which would suggest that the overall electrode reaction is

$$20H_2O + 2[SbS_4]^{3-} \rightarrow Sb_2S_3 + 5SO_4^{2-} + 40H^+ + 36e^- \quad (1)$$

but it is possible/plausible that the sulfur forms sulfite (a $26e^-/30H^+$ reaction) or thiosulfate ($16e^-/15H^+$), or some mixture of these. It is notable that whatever the sulfur oxidation product, the oxidation of $[SbS_4]^{3-}$ is a multielectron process that produces a significant number of protons and, hence, a significant local pH shift (citrate has a pK_a value of 6.4 so it is not expected that the pH will shift below this value) near the electrode's surface.

We believe that process A2 is the formation of a by-product. Process A2 arises from the direct oxidation of the $[SbS_4]^{3-}$ anion to the by-product rather than the oxidation of deposited Sb_2S_3. This was proven by scanning the potential on a glassy carbon disc from −0.15 V to 0.5 V vs SCE in the presence of $[SbS_4]^{3-}$ before ceasing the scan, rinsing the glassy carbon electrode with ultrapure water, placing the electrode into a solution of background electrolyte (no $[SbS_4]^{3-}$ present) and then scanning the potential between −0.15 V and 0.9 V vs SCE (SI, Fig. S6) whereupon no electooxidation processes was seen. Several proposed Pourbaix diagrams for antimony indicate that the formation of antimony oxide/hydroxide is possible at pH 9.1 and becomes more feasible as the potential is made more positive [36–38]. In addition, Pavlov and co-workers have suggested that antimony hydroxides formed from the electrochemical oxidation of Sb are thermodynamically unstable, and this would be consistent with the island formation observed upon annealing our deposits [39,40].

3.3. The electroreduction of the electrodeposited products

Turning now to the reduction processes. C1 and C2 only occur on the second scan, indicating that they are related to the A1 and/or A2.

If the glassy carbon electrode is swept between −0.15 and 0.9 V vs SCE in the presence of the $[SbS_4]^{3-}$ anion (so that process A1 and A2 occur), is then washed with ultrapure water, transferred to an electrolyte that does not contain the $[SbS_4]^{3-}$ anion, and then the potential is swept negative, C1 and C2 are still observed (Fig. 6). This clearly indicates that processes C1 and C2 correspond to the reduction of surface bound products of A1 and/or A2. EDX analysis obtained for electrodes that have undergone process C2 reveals that the deposits on these electrodes consist almost solely of Sb (with only small, isolated areas containing both Sb and S). This indicates that C2 corresponds to the reduction of

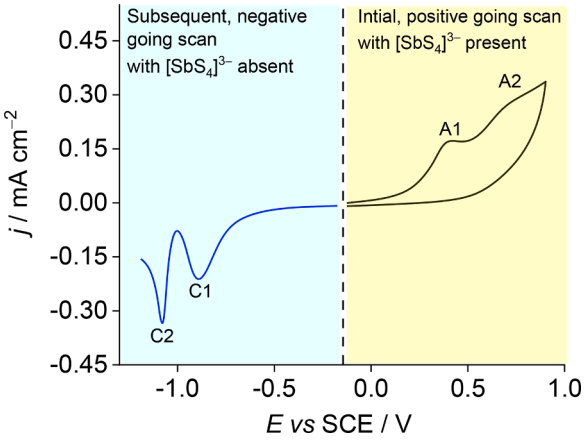

Fig. 6. Voltammetry where the potential on a glassy carbon electrode was swept between −0.15 V vs SCE and 0.9 V vs SCE at 10 mV s^{-1} in 2 mM $Na_3[SbS_4].9H_2O$ in 100 mM $HOC(COONa)(CH_2COONa)_2{\cdot}2H_2O$ (the yellow section of the figure/black trace, pH 9.1), the electrode was then rinsed with water, moved to a background electrolyte solution (pH 8.3), and the potential was swept from −0.15 V to −1.2 V vs SCE at 10 mV s^{-1} (the blue section of the figure/blue trace) (For interpretation of the references to color in this figure legend, the reader is referred to the web version of this article.).

Sb_2S_3 to elemental Sb. In simple terms this can occur according to Eq. (2) (although the process is more complicated, see Section 3.4).

$$Sb_2S_3 + 6e^- \rightarrow 2Sb + 3S^{2-} \quad (2)$$

If the negative limit is set to −0.95 V vs SCE, the EDX spectrum still shows the presence of Sb and S, suggesting process C1 is likely to be the reduction of something other than Sb_2S_3, and we therefore assign it to be the reduction of the electrodeposited by-product (thought to be an antimony oxide/hydroxide). This is supported by the observation that when the positive potential limit is set to 0.5 V vs SCE (so that only peak A1 is observed), the charge associated with C1 is much less than when the positive limit is set 0.9 V vs SCE (SI, Fig. S8). This indicates that C2 is related to A1 and that C1 is related to A2. It is clear that there is some overlap between processes A1 and A2 and it was found that if the potential was held at +0.2 V for 180 s, both C1 and C2 were observed in the subsequent negative potential scan (SI, Fig. S9). This indicates that even with a very modest overpotential for Sb_2S_3 deposition, by-product deposition can occur. A strategy for depositing pure Sb_2S_3 will be discussed in Section 3.5.

To provide additional evidence for the assignments of C1 and C2, and for comparison to the single source approach discussed in this paper, Sb_2S_3 was deposited onto a glassy carbon electrode in a more orthodox manner (separate precursors for S and for Sb, acidic conditions, cathodic potentials) [19–21]. The electrode was then rinsed with ultrapure water, transferred into a 100 mM HOC(COONa)$(CH_2COONa)_2{\cdot}2H_2O$ solution and the potential was swept negative from −0.6 V vs SCE, and two reduction peaks were observed at −0.95 V and −1.11 V vs SCE (Fig. 7), which is approximately where C1 and C2 appear in the voltammetry of $[SbS_4]^{3-}$. This voltammetry also showed a very large anodic peak related to Sb stripping (which will be discussed in greater detail in Section 3.4).

3.4. The oxidation of the products of Sb_2S_3 reduction

Fig. 8 shows that processes A3 and A4 only appear if the Sb_2S_3 deposited on the electrode has been reduced to Sb (process C2). A3 and A4 are therefore assigned to the oxidation of species formed due to C2. If a sweep is terminated after C2, at −1.2 V vs SCE, the working electrode transferred to an electrolyte that does not contain the $[SbS_4]^{3-}$ anion, and then the potential swept positive, only process A4 is observed (Fig. S10). This indicates that A4 is the oxidation of a surface species. It is known from the EDX data that C2 is the reduction of Sb_2S_3 to elemental Sb and so process A4 is therefore assigned to be the oxidation of elemental Sb according to Eq. (3). This is supported by examining the cyclic voltammetry of Sb(III) and noting that the Sb stripping occurs at the same potential (see SI, Fig. S11). This is in agreement with previous studies carried out on the voltammetry of Sb electrodes [40,41–43]

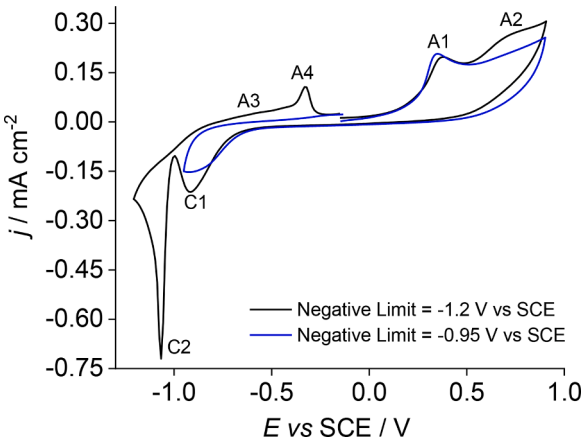

Fig. 8. Voltammograms of 2 mM $Na_3[SbS_4].9H_2O$ in 100 mM HOC(COONa)$(CH_2COONa)_2{\cdot}2H_2O$, pH 9.1, where the potential was swept from −0.15 V to 0.9 V vs SCE and then to −1.2 V (black trace) or −0.95 V (blue trace), and then back to −0.15 V vs SCE at 10 mV s^{-1} (For interpretation of the references to color in this figure legend, the reader is referred to the web version of this article.).

$$Sb \rightarrow Sb^{3+} + 3e^- \quad (3)$$

If process C2 can be fully explained by Eq. (2) one would expect the ratio of charges between C2 and A4 to be 1:1. The ratio of charges between C2 and A4 was found to be approximately 10:1, revealing that process C2 must be more complicated than a simple reduction of Sb_2S_3 to Sb and S species, and that C2 may involve processes that remove Sb from the surface of the glassy carbon electrode. One possible reaction is stibine (SbH_3) formation (Eq. (4)), which would be favoured by the lower (<9.1) pH at the electrode surface due to the significant number of protons generated at the electrode surface during reduction of $[SbS_4]^{3-}$ (Eq. (1)) and the low buffer capacity of the electrolyte at pH 9 [44]. This interpretation is supported by the observation that if the electrolyte is stirred after inducing the oxidation processes (A1 and A2) but before sweeping negative and observing C1 and C2 (hence dispersing the protons generated during oxidation of $[SbS_4]^{3-}$), the ratio of charges between C2 and A4 was found to be approximately 2:1.

$$Sb + 3H^+ + 3e^- \rightarrow SbH_3(g) \quad (4)$$

As process A3 is not observed in the voltammetry when the electrode is transferred to an electrolyte free of $[SbS_4]^{3-}$ (see SI, Fig. S10), process A3 must be a solution phase process, and is likely to be the electrochemical oxidation of soluble S species generated during process C2.

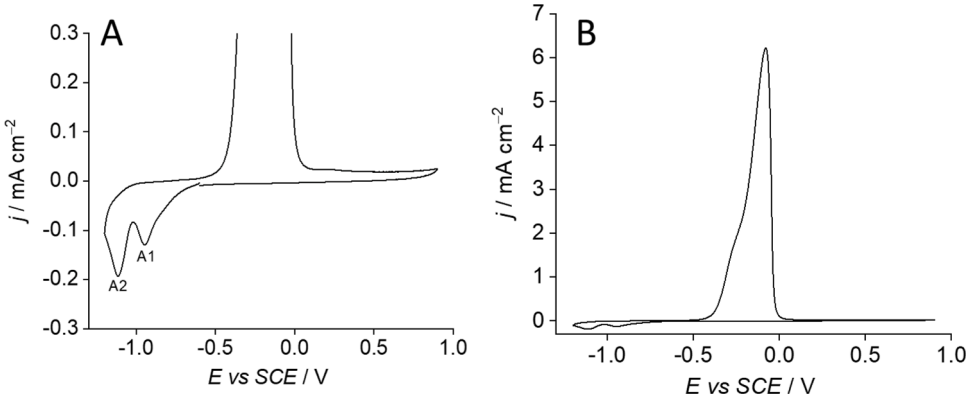

Fig. 7. Voltammograms of Sb_2S_3 on glassy carbon prepared by holding a solution of 2 mM $SbCl_3$, 10 mM $Na_2S_2O_3$, and 100 mM citric acid at −0.6 V vs SCE for 10 min. The voltammograms were obtained in 100 mM HOC(COONa)$(CH_2COONa)_2{\cdot}2H_2O$ at 10 mV s^{-1}. (a) shows the cathodic peaks of interest and (b) shows the whole voltammogram.

As previously stated, reversing the scan before C2 (Fig. 8) shows that neither A3 nor A4 are related to process C1 and shows that the reduction of the by-product formed during Sb_2S_3 deposition does not produce Sb (0) or any oxidisable solution phase S species.

To validate the assignments of these processes, Sb_2S_3 powder was drop cast onto a glassy carbon disc electrode and voltammograms were obtained to show the electrochemical behaviour of Sb_2S_3. On the first scans of the electrode from −0.15 V to −1.6 V and back to 0.9 V vs SCE at 50 mV s^{-1} the voltammetry without stirring the electrolyte (Fig. 9A) is different from the voltammetry with stirring (Fig. 9B). The voltammetry strongly resembles that shown in Fig. 1 following our electrodeposition of Sb_2S_3.

As with peak C2 in Fig. 1, Ci is assigned to be the electrochemical reduction of Sb_2S_3 to elemental Sb. This is confirmed by EDX analysis of a drop cast electrode after sweeping the potential more negative than −1.3 V vs SCE, where Sb is observed in the EDX but S is absent. As shown in Fig. S12, if the potential is not taken more negative than −1.25 V vs SCE, peaks Ai, Aii, and Aiii, are not present and are therefore dependant on process Ci, in the same way that process C2 was necessary for processes A3, A4 and A5 in Fig. 1.

Processes Ai and Aii appear in the same potential regions and have the same general shape as processes A3 and A4, respectively. Furthermore, Fig. 9B shows that when the electrolyte is stirred, peak Ai is absent but peak Aii remains, demonstrating that process Ai is a solution based electrochemical reaction and process Aii is a surface based electrochemical reaction. This is in good agreement with Fig. 1 and our results for electrodeposition from $[SbS_4]^{3-}$, lending support to the hypothesis that A3/Ai is the oxidation of soluble sulfur species produced by the reduction of Sb_2S_3 and A4/Aii is the oxidation of Sb(0) produced by the reduction of Sb_2S_3.

Process Aiii is thought to be the oxidation of Sb(0) not stripped in process Aii to antimony oxide/hydroxide as process Aiii occurs in the same potential region as Sb oxidation is reported to occur in antimony oxide/hydroxide [39,40,41]. As shown in Fig. S12, Aiii does not occur unless the potential has been swept negative of −1.25 V vs SCE, i.e. unless the Sb_2S_3 has been reduced to Sb(0), which is further evidence that Aiii is the oxidation of Sb(0).

Following the oxidation of the Sb on the electrode surface (A4) a further oxidation (A5) can be seen in the −0.1 to 0.05 V vs SCE region (Fig. 1). This is assigned to the oxidation of the remaining elemental Sb, not stripped during A3, to antimony oxide/hydroxide

$$2Sb + 3H_2O \rightarrow Sb_2O_3 + 6H^+ + 6e^- \quad (5)$$

Similar observations have been made in the literature [40–42].

From the second scan onwards, the peak potential for Sb_2S_3 deposition is shifted negative from approximately 0.36 V to approximately 0.18 V vs SCE (Fig. 1). This is likely because the overpotential required to deposit Sb_2S_3 onto Sb/Sb oxide/Sb hydroxide is lower than the overpotential required to deposit Sb_2S_3 onto glassy carbon. Table 1 summarises our assignments for the oxidation and reduction peaks.

Table 1
Assignment of the observed redox peaks in the voltammetry of $[SbS_4]^{3-}$ in Fig. 1.

Peak	Potential vs SCE / V	Assignment
A1	0.38	$[SbS_4]^{3-}$ oxidation to Sb_2S_3(s)
A2	0.73	$[SbS_4]^{3-}$ oxidation to by-product Sb_2O_3/$Sb(OH)_3$
C1	−0.92	Reduction of Sb_2O_3/$Sb(OH)_3$ to Sb(s)
C2	−1.05	Reduction of Sb_2S_3 to Sb(s) and soluble S species
A3	−0.77 to −0.40	Oxidation of soluble S species
A4	−0.32	Anodic dissolution of Sb to soluble product
A5	−0.1 to 0.05	Oxidation of remaining Sb(s)

3.5. A pulse plating strategy for the electrodeposition of pure Sb_2S_3

As discussed earlier, it is rather difficult to electrodeposit Sb_2S_3 anodically without also forming some Sb containing by-product. To overcome this problem a pulse plating strategy was devised based on the assignment of the voltammetry established above and summarised in Table 1. In this pulse plating method the electrode was pulsed at +0.4 V vs SCE to deposit Sb_2S_3 together with the by-product, then stepped to −0.95 V to reduce the by-product, and then stepped to −0.3 V to remove any Sb(0) that might be generated at −0.95 V during reduction of the by product. Each pulse was set to last 1 s and 60 pulses were taken (this is referred to as the OxRed pulse protocol). The control experiment involved pulsing for 1 s at +0.4 V vs SCE and then for 2 s at −0.15 V, the approximate open circuit potential (this is referred to as the control pulse). Fig. 10 compares voltammograms taken on glassy carbon disc electrodes after depositing Sb_2S_3 onto them following the two protocols.

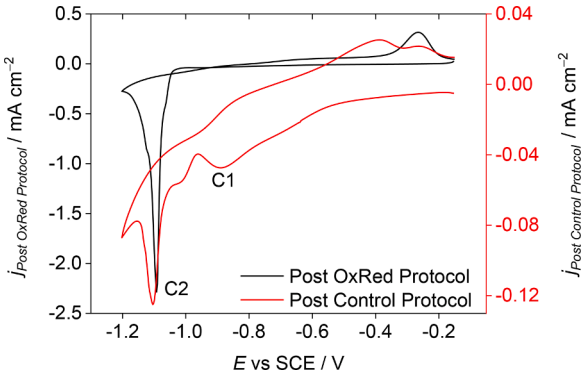

Fig. 10. Voltammograms after Sb_2S_3 electrodeposition onto glassy carbon disc electrodes following different pulse plating protocols. The potential was swept between −0.15 and −1.2 V vs SCE in background electrolyte, at 10 mV s^{-1}. The black trace (y-axis on the left) is the voltammogram of Sb_2S_3 deposited using 60 cycles of one second pulses at 0.4 V vs SCE, −0.95 V vs SCE, and −0.3 V vs SCE (OxRed pulse protocol), the red trace (y-axis on the right) is for Sb_2S_3 deposited using 60 cycles of one second pulses at 0.4 V vs SCE and a two second pulses at −0.15 V vs SCE (control pulse protocol).

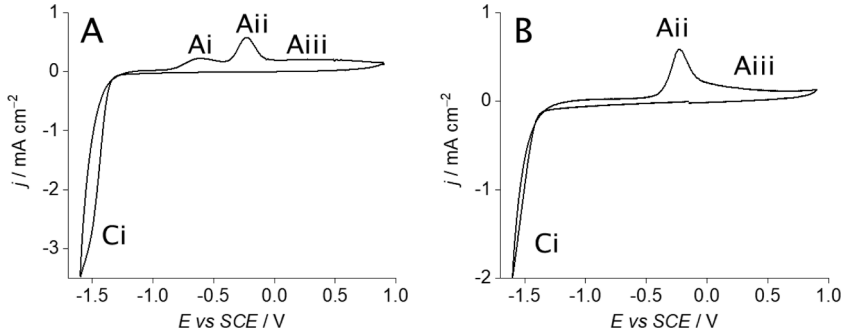

Fig. 9. Voltammetry of Sb_2S_3 drop cast onto a GC electrode in 100 mM $HOC(COONa)(CH_2COONa)_2{\cdot}2H_2O$, pH 8.3. A) without stirring and B) with stirring. The scan rate is 50 mV s^{-1}.

Note that C1 is only observed for the electrode that was subjected to the control protocol, showing that the OxRed protocol is an effective way of obtaining Sb_2S_3 without the by product.

Interestingly, the current associated with Sb_2S_3 reduction to Sb(0) after the control protocol is much smaller than that of the OxRed protocol (Fig. 10) even though the total time spent at the deposition potential (0.4 V vs SCE) was the same in both cases. Integration of the reduction peak at −1.1 V vs SCE shows that approximately 760 μC of charge is passed during the Sb_2S_3 reduction during the OxRed protocol, whereas only approximately 75 μC has been passed after the control pulse protocol. This suggests that the formation of the by-product retards the anodic electrodeposition of Sb_2S_3 so that, in addition to pulse plating between processes A1, C1 and A4 being necessary to produce pure Sb_2S_3 deposits, it is also helpful for deposition of thicker films. This is consistent with previously published literature, in which it was reported that the formation of Sb oxides can passivate an electrode's surface [39,40,44]

3.6. *Screening electrodeposited films for resistive random-access memory applications*

The electronic switching properties of the electrodeposited Sb_2S_3-films were investigated for application in RRAM. Annealed films deposited under constant potential and by pulsed potential were studied and no diferences were observed between the two. In the following current-voltage (*I-V*) measurements were carried out on devices fabricated using Sb_2S_3 films on glassy carbon plates prepared by holding the potential at 1 V vs SCE for 600 s in 2 mM $Na_3[SbS_4].9H_2O$ in 100 mM of sodium citrate tribasic dihydrate. The resulting deposits were then annealed at 350 °C and 0.1 mbar under a sulfur rich environment. The devices were measured under an external applied voltage that was swept between −4 V and 3.5 V, as shown in Fig. 11a. The glassy carbon substrate and tungsten probe (5 μm in diameter) were used as bottom and top contacts, respectively (see the inset for Fig. 11a). It is worth noting that no forming process was needed to initiate the devices for resistive switching. As shown in Fig. 11a, the device shows typical bipolar resistive switching behaviour between a HRS and an LRS. The direction of the current sweep is indicated by arrows. The device is initially in a high resistance state. By applying a negative sweep voltage (from 0 V to −4 V), the device switched from the HRS to LRS at a SET voltage of approximately −3.6 V. The device remained in its LRS during the backward sweep voltage (from −4 V to 0 V). However, during the subsequent positive sweep voltage (from 0 V to 3.5 V), the device switched from the LRS to HRS at a RESET voltage of approximately 3.3 V and then remained in its HRS when reversing the positive sweep voltage (from 3.5 V to 0 V). The sharp switching observed from the HRS to LRS indicates that the switching is filamentary based [45]. Fig. 11b shows a reproducible cycling endurance in the DC sweep mode for 50 cycles. The resistance ratio between the HRS and the LRS is about 1 order of magnitude at 1.5 V, which is sufficient for memory applications. Both the HRS and the LRS showed excellent uniformity without significant degradation. To further elucidate the switching stability of the device, cumulative probability distributions for the HRS and the LRS were obtained and are shown in Fig. 11c. Fig. 11c clearly shows that the HRS and LRS are uniformly distributed with the coefficients of the variation (σ/μ, where σ is the standard deviation and μ is the mean value) calculated to be 4.08% and 1.38% for the HRS and LRS, respectively. Furthermore, high uniformities were also observed for both V_{SET} and V_{RESET} as shown in Fig. 11d, where the coefficients of the variation were 0.355% and 0.237%, respectively. The high uniformities of both programming voltages are essential for large-scale RRAM applications.

In Fig. 12a, the conduction mechanism of the electrodeposited Sb_2S_3 RRAM device was examined by plotting the negative part of the *I-V* curve on a log − log scale. The fit suggests that the conduction mechanism is governed by the Space-Charge-Limited-Current (SCLC) model [24,46]. Initially from 0 V to 0.45 V at HRS, the device shows a linear dependence of current with applied voltage ($I \propto V$), with a slope of about 1. This is attributed to an Ohmic conduction mechanism, which arises from thermally generated charge carriers [46–48]. At higher applied voltages ($0.5 \leq V \leq 2.4$ V) the slope changes to approximately 2, and the current exhibits the voltage square dependence ($I \propto V^2$), which can be attributed to the trap-controlled space charge limited current (TC-SCLC). In the region of $2.45 \leq V \leq 3.45$ V, a much steeper rate of current increase occurs ($I \propto V^{\alpha}$, $\alpha \approx 6$), indicating that all traps are filled,

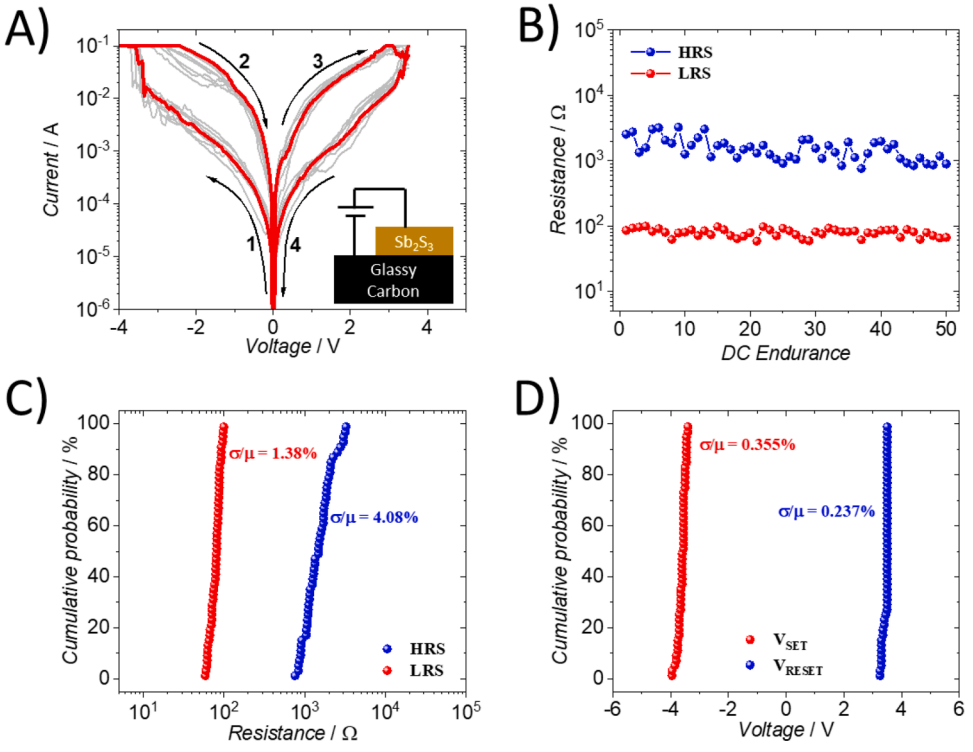

Fig. 11. Resistive switching properties of the electrochemically deposited Sb_2S_3 RRAM devices. (a) Consecutive bipolar *I–V* characteristics. The inset shows the schematic of the device. (b) Endurance characteristics. (c) Cumulative probability of HRS and LRS. (d) Cumulative probability of V_{SET} and V_{RESET}. Sb_2S_3 RRAM devices prepared b yholding the potential on a glassy carbon plate at 1 V vs SCE for 600 s in 2 mM $Na_3[SbS_4].9H_2O$ in 100 mM HOC $(COONa)(CH_2COONa)_2 \cdot 2H_2O$, pH 9.1, and then annealing the resulting deposits at 350 °C and 0.1 mbar under a sulfur rich environment.

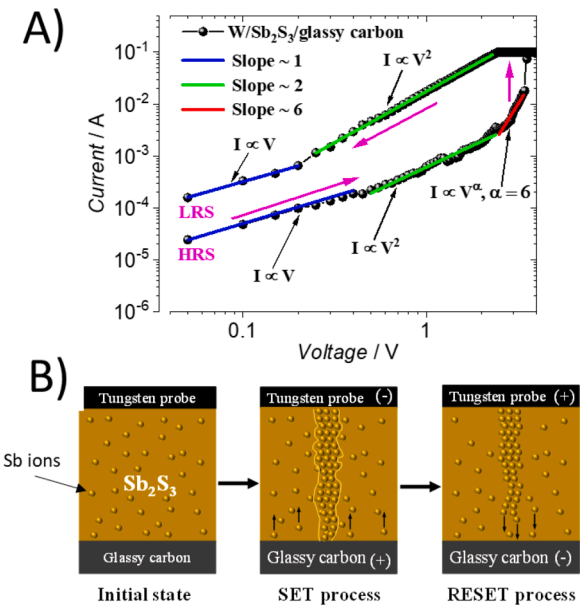

Fig. 12. (a) *I–V* curve fitting using an SCLC model on a glassy carbon/Sb_2S_3/W RRAM device. (b) Schematic showing the resistive switching mechanism in Sb_2S_3-based RRAM devices. Sb_2S_3 RRAM devices were prepared as in Fig. 11.

and the conduction mechanism is ascribed to trap-filled space charge limited conduction (TF-SCLC). At the threshold of 3.5 V, a sharp transition in the current occurs, switching the device from the HRS to the LRS. In the case of the LRS, the conduction mechanism is dominated by two regions: Ohmic conduction at low applied voltage, featuring the linear dependence of current with applied voltage, ($I \propto V$), and SCLC at higher voltage, where the current shows the voltage square dependence, ($I \propto V^2$).

The resistive switching mechanism of the electrodeposited Sb_2S_3 RRAM device can be ascribed to the solid-state electrolyte effect of the Sb_2S_3. The solid-state electrolyte effect (also called electrochemical metallisation) is a commonly proposed switching mechanism in Sb-rich and Te-rich GeSbTe chalcogenide alloys [24,49,50]. Application of an external electric field causes oxidation/reduction reactions at the interfaces, resulting in ionic conduction. When a sufficient electric field is applied in one polarity, Sb conductive filaments are formed across the Sb_2S_3 thin film, switching the device to the LRS. In contrast, reversing the polarity of the applied electric field dissolves the formed filaments, due to movement of ions in the opposite direction, switching the device back into its HRS. In Fig. 12b the schematic of the proposed switching mechanism is presented. A large amount of Sb atoms are available in the electrodeposited Sb_2S_3 matrix for the device in its initial state. In the literature, Sb is a cation-like species in alloys, therefore it can ionize and move upon application of a sufficient electric field [51]. Application of a negative potential to the top electrode attracts the cationic Sb species to the top electrode, where neutral Sb atoms are accumulated and start to form a filament. Once the grown filament reaches the bottom electrode, the device switches to the LRS (SET process). In contrast, upon reversing the polarity of applied potential, the cationic Sb species move to the bottom electrode and dissolve the preformed filament, switching the device back to the HRS (RESET process).

4. Conclusions

The electrochemistry of the $[SbS_4]^{3-}$ anion has been thoroughly characterised by voltammetry. It has been found that an amorphous film of Sb_2S_3 can be anodically electrodeposited onto glassy carbon from $[SbS_4]^{3-}$ in aqueous solution at pH 9.1. This deposition is accompanied by co-deposition of a by-product that is thought to be antimony oxide/hydroxide. Cathodic biases can then be used to reduce both the Sb_2S_3 and the oxide/hydroxide by-products to Sb(0). By switching the potential between the positive potential at which Sb_2S_3 and antimony oxide/hydroxide is formed and the negative potential at which only antimony oxide/hydroxide is reduced, a film of pure Sb_2S_3 can be obtained. The amorphous films can be crystalized by annealing.

The annealed films showed typical bipolar resistive switching behaviour, and displayed a resistance ratio of HRS:LRS of approximately one order of magnitude at 1.5 V, which is suitable for memory applications. This switching behaviour is ascribed to the formation and rupture of Sb ion-based filaments within the Sb_2S_3 matrix.

CRediT authorship contribution statement

A.G. Wallace: Conceptualization, Methodology, Investigation, Validation, Formal analysis, Writing – original draft. **R.P. King:** Conceptualization, Methodology, Resources, Writing – review & editing. **N. Zhelev:** Methodology, Writing – review & editing. **A.H. Jaafar:** Conceptualization, Methodology, Investigation, Validation, Formal analysis, Writing – original draft. **W. Levason:** Conceptualization, Methodology, Resources, Writing – review & editing. **R. Huang:** Conceptualization, Methodology, Writing – review & editing. **G. Reid:** Methodology, Conceptualization, Resources, Writing – review & editing. **P.N. Bartlett:** Conceptualization, Methodology, Validation, Formal analysis, Writing – review & editing, Supervision, Funding acquisition, Project administration.

Declaration of Competing Interest

The authors declare that they have no known competing financial interests or personal relationships that could have appeared to influence the work reported in this paper.

Data Availability

Data will be made available on request.

Acknowledgements

This work was supported by EPSRC Grants EP/N035437/1 and EP/K009877/1.

Supplementary materials

Supplementary material associated with this article can be found, in the online version, at doi:10.1016/j.electacta.2022.141162.

References

[1] R.G. Sotelo Marquina, T.G. Sanchez, N.R. Mathews, X. Mathew, Vacuum coated Sb_2S_3 thin films: thermal treatment and the evolution of its physical properties, Mater. Res. Bull. 90 (2017) 285–294, https://doi.org/10.1016/j.materresbull.2017.03.013.

[2] L. Zhang, C. Wu, W. Liu, S. Yang, M. Wang, T. Chen, C. Zhu, Sequential deposition route to efficient Sb_2S_3 solar cells, J. Mater. Chem. A 6 (2018) 21320–21326, https://doi.org/10.1039/c8ta08296k.

[3] R. Boughalmi, A. Boukhachem, M. Kahlaoui, H. Maghraoui, M. Amlouk, Physical investigations on Sb_2S_3 sprayed thin film for optoelectronic applications, Mater. Sci. Semicond. Process. 26 (2014) 593–602, https://doi.org/10.1016/j.mssp.2014.05.059.

[4] P. Makreski, G. Petruševski, S. Ugarković, G. Jovanovski, Laser-induced transformation of stibnite (Sb_2S_3) and other structurally related salts, Vib. Spectrosc. 68 (2013) 177–182, https://doi.org/10.1016/j.vibspec.2013.07.007.

[5] K.F. Abd-El-Rahman, A.A.A. Darwish, Fabrication and electrical characterization of p-Sb_2S_3/n-Si heterojunctions for solar cells application, Curr. Appl. Phys. 11 (2011) 1265–1268, https://doi.org/10.1016/j.cap.2010.12.006.

[6] F. Aousgi, M. Kanzari, Study of the optical properties of Sn-doped Sb_2S_3 thin films, Energy Procedia 10 (2011) 313–322, https://doi.org/10.1016/j.egypro.2011.10.197.

[7] J. He, Y. Wei, T. Zhai, H. Li, Antimony-based materials as promising anodes for rechargeable lithium-ion and sodium-ion batteries, Mater. Chem. Front. 2 (2018) 437–455, https://doi.org/10.1039/c7qm00480j.

[8] C.M. Park, Y. Hwa, N.E. Sung, H.J. Sohn, Stibnite (Sb_2S_3) and its amorphous composite as dual electrodes for rechargeable lithium batteries, J. Mater. Chem. 20 (2010) 1097–1102, https://doi.org/10.1039/b918220a.

[9] S. Yao, J. Cui, Z. Lu, Z.L. Xu, L. Qin, J. Huang, Z. Sadighi, F. Ciucci, J.K. Kim, Unveiling the unique phase transformation behavior and sodiation kinetics of 1D van der Waals Sb_2S_3 anodes for sodium ion batteries, Adv. Energy Mater. 7 (2017) 1–11, https://doi.org/10.1002/aenm.201602149.

[10] S. Dembele, A. Akcil, S. Panda, Technological trends, emerging applications and metallurgical strategies in antimony recovery from stibnite, Miner. Eng. 175 (2022), 107304, https://doi.org/10.1016/j.mineng.2021.107304.

[11] S.S. Karade, K. Banerjee, S. Majumder, B.R. Sankapal, Novel application of non-aqueous chemical bath deposited Sb_2S_3 thin films as supercapacitive electrode, Int. J. Hydrog. Energy. 41 (2016) 21278–21285, https://doi.org/10.1016/j.ijhydene.2016.07.196.

[12] X. Wang, R. Tang, C. Wu, C. Zhu, T. Chen, Development of antimony sulfide–selenide $Sb_2(S,Se)_3$-based solar cells, J. Energy Chem. 27 (2018) 713–721, https://doi.org/10.1016/j.jechem.2017.09.031.

[13] P. Zhong, J. Xie, R. Bagheri, Q. Yi, Q. Chen, J. Tan, L. He, F. Zhang, L. Zhang, G. Zou, An aqueous solution method towards Sb_2S_3 thin films for photoanodes, Chem. Commun. 55 (2019) 14530–14533, https://doi.org/10.1039/c9cc07005b.

[14] I.H. Baek, J.J. Pyeon, Y.G. Song, T.M. Chung, H.R. Kim, S.H. Baek, J.S. Kim, C. Y. Kang, J.W. Choi, C.S. Hwang, J.H. Han, S.K. Kim, Synthesis of SnS thin films by atomic layer deposition at low temperatures, Chem. Mater. 29 (2017) 8100–8110, https://doi.org/10.1021/acs.chemmater.7b01856.

[15] C. Gao, J. Huang, H. Li, K. Sun, Y. Lai, M. Jia, L. Jiang, F. Liu, Fabrication of Sb_2S_3 thin films by sputtering and post-annealing for solar cells, Ceram. Int. 45 (2019) 3044–3051, https://doi.org/10.1016/j.ceramint.2018.10.155.

[16] Y.C. Choi, S. Il Seok, Efficient Sb_2S_3-sensitized solar cells via single-step deposition of Sb_2S_3 using S/Sb-ratio-controlled $SbCl_3$-thiourea complex solution, Adv. Funct. Mater. 25 (2015) 2892–2898, https://doi.org/10.1002/adfm.201500296.

[17] H. Deng, S. Yuan, X. Yang, F. Cai, C. Hu, K. Qiao, J. Zhang, J. Tang, H. Song, Z. He, Efficient and stable TiO_2/Sb_2S_3 planar solar cells from absorber crystallization and Se-atmosphere annealing, Mater. Today Energy 3 (2017) 15–23, https://doi.org/10.1016/j.mtener.2017.02.001.

[18] M.A. de Araújo, F.W.S. Lucas, L.H. Mascaro, Effect of the electrodeposition potential on the photoelectroactivity of the SnS/Sb_2S_3 thin films, J. Solid State Electrochem. 24 (2020) 389–399, https://doi.org/10.1007/s10008-020-04508-2.

[19] R.G. Avilez Garcia, C.A. Meza Avendaño, M. Pal, F. Paraguay Delgado, N. R. Mathews, Antimony sulfide (Sb_2S_3) thin films by pulse electrodeposition: effect of thermal treatment on structural, optical and electrical properties, Mater. Sci. Semicond. Process. 44 (2016) 91–100, https://doi.org/10.1016/j.mssp.2015.12.018.

[20] N.S. Yesugade, C.D. Lokhande, C.H. Bhosale, Structural and optical properties of electrodeposited Bi_2S_3, Sb_2S_3 and As_2S_3 thin films, Thin Solid Films 263 (1995) 145–149, https://doi.org/10.1016/0040-6090(95)06577-6.

[21] F. Tlig, M. Gannouni, I. Ben Assaker, R. Chtourou, New investigation on the physical and electrochemical properties of (TAS) thin films grown by electrodeposition technique, J. Photochem. Photobiol. A Chem. 335 (2017) 26–35, https://doi.org/10.1016/j.jphotochem.2016.11.013.

[22] S.J. Reeves, Y.J. Noori, W. Zhang, G. Reid, P.N. Bartlett, Chloroantimonate electrochemistry in dichloromethane, Electrochim. Acta 354 (2020), 136692, https://doi.org/10.1016/j.electacta.2020.136692.

[23] G.P. Kissling, R. Huang, A. Jolleys, S.L. Benjamin, A.L. Hector, G. Reid, W. Levason, C.H.(Kees) de Groot, P.N. Bartlett, Electrodeposition of a functional solid state memory material: germanium antimony telluride from a non-aqueous plating bath, J. Electrochem. Soc. 165 (2018) D557–D567, https://doi.org/10.1149/2.0981811jes.

[24] A.H. Jaafar, L. Meng, Y.J. Noori, W. Zhang, Y. Han, R. Beanland, D.C. Smith, G. Reid, K. De Groot, R. Huang, P.N. Bartlett, Electrodeposition of GeSbTe-based resistive switching memory in crossbar arrays, J. Phys. Chem. C 125 (2021) 26247–26255, https://doi.org/10.1021/acs.jpcc.1c08549.

[25] R. Huang, K. Sun, K.S. Kiang, K.A. Morgan, C.H. De Groot, Forming-free resistive switching of tunable ZnO films grown by atomic layer deposition, Microelectron. Eng. 161 (2016) 7–12, https://doi.org/10.1016/j.mee.2016.03.038.

[26] A.H. Jaafar, M. O'Neill, S.M. Kelly, E. Verrelli, N.T. Kemp, Percolation threshold enables optical resistive-memory switching and light-tuneable synaptic learning in segregated nanocomposites, Adv. Electron. Mater. 5 (2019), https://doi.org/10.1002/aelm.201900197.

[27] D.I. Son, D.H. Park, J. Bin Kim, J.W. Choi, T.W. Kim, B. Angadi, Y. Yi, W.K. Choi, Bistable organic memory device with gold nanoparticles embedded in a conducting poly(N -vinylcarbazole) colloids hybrid, J. Phys. Chem. C 115 (2011) 2341–2348, https://doi.org/10.1021/jp110030x.

[28] M.J. Lee, C.B. Lee, D. Lee, S.R. Lee, M. Chang, J.H. Hur, Y.B. Kim, C.J. Kim, D. H. Seo, S. Seo, U.I. Chung, I.K. Yoo, K. Kim, A fast, high-endurance and scalable non-volatile memory device made from asymmetric Ta_2O_{5-xx}/TaO_{2-x} bilayer structures, Nat. Mater. 10 (2011) 625–630, https://doi.org/10.1038/nmat3070.

[29] V.K. Nagareddy, M.D. Barnes, F. Zipoli, K.T. Lai, A.M. Alexeev, M.F. Craciun, C. D. Wright, Multilevel ultrafast flexible nanoscale nonvolatile hybrid graphene oxide-titanium oxide memories, ACS Nano 11 (2017) 3010–3021, https://doi.org/10.1021/acsnano.6b08668.

[30] T. Kim, S. Lee, Evolution of phase-change memory for the storage-class memory and beyond, IEEE Trans. Electron. Devices 67 (2020) 1394–1406, https://doi.org/10.1109/TED.2020.2964640.

[31] G. Brauer, Handbook of Preparative Inorganic Chemistry, 2nd ed., 1, Academic Press, New York, 1963.

[32] P. Bayliss, W. Nowacki, Refinement of the crystal structure of stibnite, Sb_2S_3, Z. Krist. 315 (1972) 308–315.

[33] J.S. Eensalu, K. Tõnsuaadu, I. Oja Acik, M. Krunks, Sb_2S_3 thin films by ultrasonic spray pyrolysis of antimony ethyl xanthate, Mater. Sci. Semicond. Process. 137 (2022), 106208, https://doi.org/10.1016/j.mssp.2021.106209.

[34] M.A. Williamson, J.D. Rimstidt, Correlation between structure and thermodynamic properties of aqueous sulfur species, Geochim. Cosmochim. Acta 56 (1992) 3867–3880, https://doi.org/10.1016/0016-7037(92)90002-Z.

[35] R.M. Garrels, C.R. Naeser, Equilibrium distribution of dissolved sulphur species in water at 25 °C and 1 atm total pressure, Geochim. Cosmochim. Acta. 15 (1950) 113–130, https://doi.org/10.1016/0016-7037(58)90014-0.

[36] J. Segura-Salazar, P.R. Brito-Parada, Stibnite froth flotation: a critical review, Miner. Eng. 163 (2021), 106713, https://doi.org/10.1016/j.mineng.2020.106713.

[37] K.M. Krupka, R.J. Serne. Geochemical Factors Affecting the Behavior of Antimony, Cobalt, Europium, Technetium, and Uranium in Vadose Zone Sediments, U.S. Department of Energy, United States, 2002. https://www.pnnl.gov/main/publications/external/technical_reports/PNNL-14126.pdf.

[38] M. Filella, N. Belzile, Y.W. Chen, Antimony in the environment: a review focused on natural waters. Part 2. Relevant solution chemistry, ChemInform 34 (2003) 265–285, https://doi.org/10.1002/chin.200323280.

[39] D. Pavolv, M. Bojinov, T. Laitinen, G. Sundholm, Electrochemical behaviour of the antimony electrode in sulphuric acid solutions-I. Corrosion prosesses and anodic dissolution of antimony, Electrochim. Acta 36 (1991) 2081–2086.

[40] D. Pavlov, M. Bojinov, T. Laitinen, G. Sundholm, Electrochemical behaviour of the antimony electrode in sulphuric acid solutions-II. Formation and properties of the primary anodic layer, Electrochim. Acta 36 (1991) 2087–2092, https://doi.org/10.1016/0013-4686(91)85214-R.

[41] M. Metikoš-Huković, R. Babić, S. Omanović, Electrochemical kinetics of anodic layer formation and reduction on antimony and antimonial lead, J. Electroanal. Chem. 374 (1994) 199–206, https://doi.org/10.1016/0022-0728(94)03354-4.

[42] B. Sebez, B. Ogorevc, S.B. Hocevar, M. Veber, Functioning of antimony film electrode in acid media under cyclic and anodic stripping voltammetry conditions, Anal. Chim. Acta 785 (2013) 43–49, https://doi.org/10.1016/j.aca.2013.04.051.

[43] X. Shi, X. Zhang, C. Ma, C. Wang, Kinetic studies of underpotential deposition of antimony on Se-modified Au electrode, J. Solid State Electrochem. 14 (2010) 93–99, https://doi.org/10.1007/s10008-009-0793-6.

[44] V. Past, A.J. Bard, Encyclopedia of electrochemistry of the elements Volume IV, ed., in: Encyclopedia of Electrochemical, IV, Marcel Dekker, New York, 1975, pp. 32–35. Vol

[45] D.J. Wouters, R. Waser, M. Wuttig, Phase-change and redox-based resistive switching memories, Proc. IEEE 103 (2015) 1274–1288, https://doi.org/10.1109/JPROC.2015.2433311.

[46] A.H. Jaafar, R.J. Gray, E. Verrelli, M. O'Neill, S.M. Kelly, N.T. Kemp, Reversible optical switching memristors with tunable STDP synaptic plasticity: a route to hierarchical control in artificial intelligent systems, Nanoscale 9 (2017) 17091–17098, https://doi.org/10.1039/c7nr06138b.

[47] R. Huang, X. Yan, K.A. Morgan, M.D.B. Charlton, C.H. De Groot, Selection by current compliance of negative and positive bipolar resistive switching behaviour in ZrO_{2-x}/ZrO_2 bilayer memory, J. Phys. D Appl. Phys. 50 (2017), 175101, https://doi.org/10.1088/1361-6463/aa64bc.

[48] A.H. Jaafar, A. Gee, N.T. Kemp, Nanorods versus nanoparticles: a comparison study of Au/ZnO-PMMA/Au non-volatile memory devices showing the importance of nanostructure geometry on conduction mechanisms and switching properties, IEEE Trans. Nanotechnol. 19 (2020) 236–246, https://doi.org/10.1109/TNANO.2019.2949759.

[49] R. Pandian, B.J. Kooi, J.L.M. Oosthoek, P. Van Den Dool, G. Palasantzas, A. Pauza, Polarity-dependent resistance switching in GeSbTe phase-change thin films: the importance of excess Sb in filament formation, Appl. Phys. Lett. 95 (2009), 252109, https://doi.org/10.1063/1.3276272.

[50] R. Pandian, B.J. Kooi, G. Palasantzas, J.T.M. De Hosson, A. Pauza, Polarity-dependent reversible resistance switching in Ge-Sb-Te phase-change thin films, Appl. Phys. Lett. 91 (2007), 152103, https://doi.org/10.1063/1.2798242.

[51] S. Yoo, T. Eom, T. Gwon, C.S. Hwang, Bipolar resistive switching behavior of an amorphous $Ge_2Sb_2Te_5$ thin films with a Te layer, Nanoscale 7 (2015) 6340–6347, https://doi.org/10.1039/c5nr01361e.